Unsupervised clustering of Southern Ocean Argo float temperature profiles

Daniel C. Jones[1], **Harry J. Holt**[1,2], **Andrew J.S. Meijers**[1], **Emily Shuckburgh**[1]

[1]British Antarctic Survey, Cambridge, UK

[2]Department of Physics, University of Cambridge, Cambridge, UK

Key Points:

- We apply Gaussian mixture modeling (GMM) to Southern Ocean temperature data
- GMM identifies spatially coherent profile types without using latitude or longitude information
- GMM offers a complementary approach for objectively classifying temperature profiles

Corresponding author: D. C. Jones, `dannes@bas.ac.uk`

Abstract

The Southern Ocean has a complex density structure characterized by sharp fronts, steeply tilted isopycnals, and deep seasonal mixed layers. Methods of defining Southern Ocean density structures traditionally rely on somewhat ad-hoc combinations of physical, chemical, and dynamic properties. As a step towards an alternative approach for defining water masses, here we apply an unsupervised classification technique (that is, Gaussian mixture modelling or GMM) to Southern Ocean Argo float temperature profiles. GMM, without using any latitude or longitude information, automatically identifies several circumpolar classes influenced by the Antarctic Circumpolar Current. In addition, GMM identifies classes that bear the imprint of mode/intermediate water formation and export, large-scale gyre circulation, and the Agulhas Current, among others. Because GMM is robust, standardized, and automated, it can potentially be used to identify structures in both observational and model datasets, possibly making it a useful complement to existing classification techniques.

Plain Language Summary

The Southern Ocean is an important part of the climate system, in part because it absorbs a large fraction of the heat and carbon that is added to the atmosphere/ocean system by human-driven fossil fuel burning. In this work, we use a machine learning technique to automatically sort Southern Ocean temperature measurements into groups based on how those temperature measurements change with depth. Different groups have the fingerprints of different large-scale circulation patterns, such as the powerful Antarctic Circumpolar Current that flows around Antarctica. The groups that we identify are consistent with our understanding of the Southern Ocean, which gives us confidence that our machine learning technique may be useful for automatically grouping measurements and computer model data in the future. This matters because the climate science community needs a new set of tools, possibly including the machine learning technique that we use in this paper, to deal with a very large, ever-increasing volume of observational and computer model data.

1 Introduction

The Southern Ocean is a critical component of Earth's climate system, having thus far absorbed greater than 75% of the energy added via anthropogenic emissions and 50% of the excess carbon [*Fletcher et al.*; *Frölicher et al.*, 2015]. Its ability to absorb heat and carbon comes in part from its unique density structure and circulation, which features upwelling of cold, nutrient rich waters and regions of dense water formation [*Lumpkin and Speer*, 2007]. Characterizing and understanding the mean state and variability of Southern Ocean density structure remains an important and climatically-relevant goal of modern oceanography.

Through decades of effort, the oceanographic community has converged on a description of ocean structure that uses temperature, salinity, dynamical, and biogeochemical patterns to define different water masses (e.g. using potential vorticity minima to locate mode water pools) [*Talley*, 2013, and references therein]. These systematic approaches employ the understanding that water mass properties are "set" in their formation regions and modified by advection, mixing, and biogeochemical processes. This modern classification scheme is extremely useful and will continue to be useful well into the future, but it is not necessarily ideal for every application. Many of the temperature, salinity, and density values used to delimit one water mass from another are somewhat ad-hoc and very specific (e.g. boundaries between different types of mode water). These schemes are useful for observational data analysis but difficult to apply to numerical models of the ocean, which do not necessarily feature exactly the same structure as the observed ocean [*Sallée et al.*, 2013]. It is therefore prudent to develop and test alternative methods for the classification of different oceanic temperature, salinity, and density structures, as a complement to existing expertise-driven methods.

Maze et al. [2017] have shown that Argo temperature profile data from the North Atlantic Ocean can be usefully grouped into classes using Gaussian mixture modelling (GMM), an unsupervised classification technique. GMM describes the spatial structure of Argo profiles as a collection of Gaussian modes whose means and standard deviations generally vary with pressure. In this work, we apply GMM to Southern Ocean Argo temperature profiles in the upper 1000 m of the water column. We find that GMM identifies several circumpolar classes, gyres, the Agulhas current, and pathways broadly associated with the formation and export of mode and intermediate waters. In section 2, we describe the Argo dataset and the basics of GMM. In section 3, we present the results of applying GMM to Southern Ocean

Argo data, and in sections 4 and 5 we offer a brief discussion and summarize our conclusions.

2 Methods

We applied an unsupervised classification method (i.e. Gaussian mixture modelling, hereafter GMM) to Southern Ocean Argo float data. In this section, we briefly describe the Argo dataset and the basics of GMM. We use the *scikit-learn* machine learning library for Python (`http://scikit-learn.org/`), and the source code used for much of the analysis in this paper is available via Github (`https://github.com/DanJonesOcean/OceanClustering`). We refer the reader to *Maze et al.* [2017] for further detail on applying GMM to Argo float data.

2.1 Argo float dataset

Argo floats are autonomous ocean instruments that measure, at minimum, the temperature and salinity of the ocean by periodically taking vertical profiles. Every 10 days, starting at a "neutral" position of 1000 m, an Argo float dives down to 2000 m before rising to the surface, taking a vertical profile of the water column along the way. The measurements are transmitted via satellite and are ultimately made freely available via the Argo Global Data Assembly Centers (GDACs) after some quality control checks. At the time of this writing, over 3800 Argo floats are active in the global ocean, producing over 100,000 temperature and salinity profiles per year with an average spacing of 3° (`http://www.argo.ucsd.edu/`).

For this study, we selected all available Argo profiles south of 30°S that have been flagged by the GDACs as "observation good" (i.e. quality control flag = 1) covering the time period from 2001 to early 2017. More specifically, we used a vertically interpolated product with 400 pressure levels ranging from 0 to 2000 dbar. After discarding profiles with greater than or equal to 6% NaN values (2% of the initial number of profiles) and discarding pressure levels with greater than or equal to 3% NaN values, we were left with 284,427 profiles, each with 192 pressure levels between 15 dbar and 980 dbar. We replaced all remaining NaN values ($\ll$ 1% of the total temperature measurements) with linearly interpolated estimates using nearest neighbor values. We refer to the resulting dataset as the cleaned dataset.

Because of the autonomous and free-drifting nature of the floats, the profiles are not distributed evenly in latitude/longitude (Figure 1). The profiles are more heavily concentrated in the Pacific sector (roughly 890 profiles per degree longitude, totalling 47% of profiles) and Indian sector (800 profiles per degree longitude, totalling 34% of profiles), with relatively fewer profiles in the Atlantic sector (610 profiles per degree longitude, 19% of total). When counted in equal-area bins and plotted by latitude, we see that the number or profiles decreases towards Antarctica (Figure 1(b)), which is partly due to challenging operational conditions associated with seasonal sea ice, which can extend to just north of 60°S at maximum areal extent. The profiles are slightly over-represented in the Austral summer and autumn (DJF-MAM, 52% of profiles) and under-represented in the Austral winter and spring (JJA-SON, 48% of profiles), and the number of profiles increases until 2013 (Figure 1(c,d)). Since we selected an Argo dataset that was created in early 2017, there are relatively few profiles from that year.

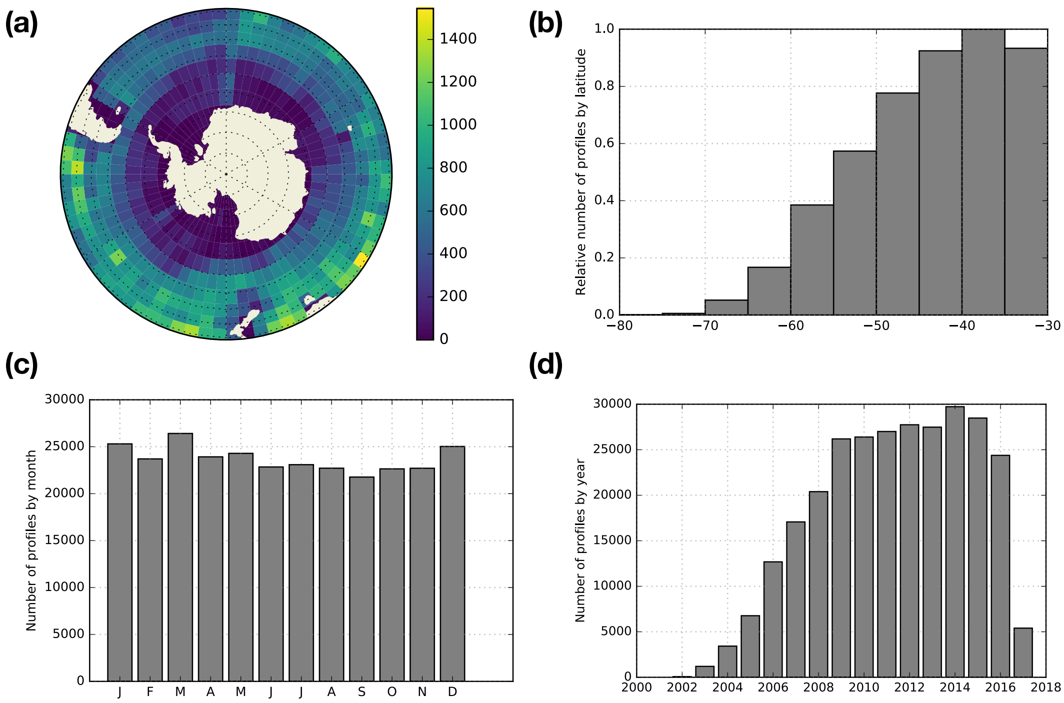

Figure 1. Distribution of Argo temperature profiles from the cleaned dataset. (a) Number of profiles in $5^\circ \times 5^\circ$ bins. (b) Relative number of profiles by latitude, scaled by an area-weighting factor $\cos(\phi)$, where ϕ is latitude. The temporal distribution of profiles shown by (c) month and (d) year.

The profiles selected for this study display a large variety of vertical temperature structures (Figure 2). The range of temperatures is wider in the surface and considerably narrower with pressure, in part reflecting the seasonal cycle in upper ocean temperatures. A large number of profiles feature colder temperatures near the surface and warmer temperatures in the interior, a physical arrangement that would be unstable to convection without the compensating effect of salinity. Water masses around Antarctica tend to be fresher at the surface and saltier in the interior due to glacial melt, freshwater flux, and the balance of evaporation/precipitation. This arrangement of temperature and salinity can be stable to vertical mixing (called “salt stratification"). In addition, the thermocline, i.e. the region of the ocean that features a rapid change in temperature with pressure, is visible in some temperature profiles.

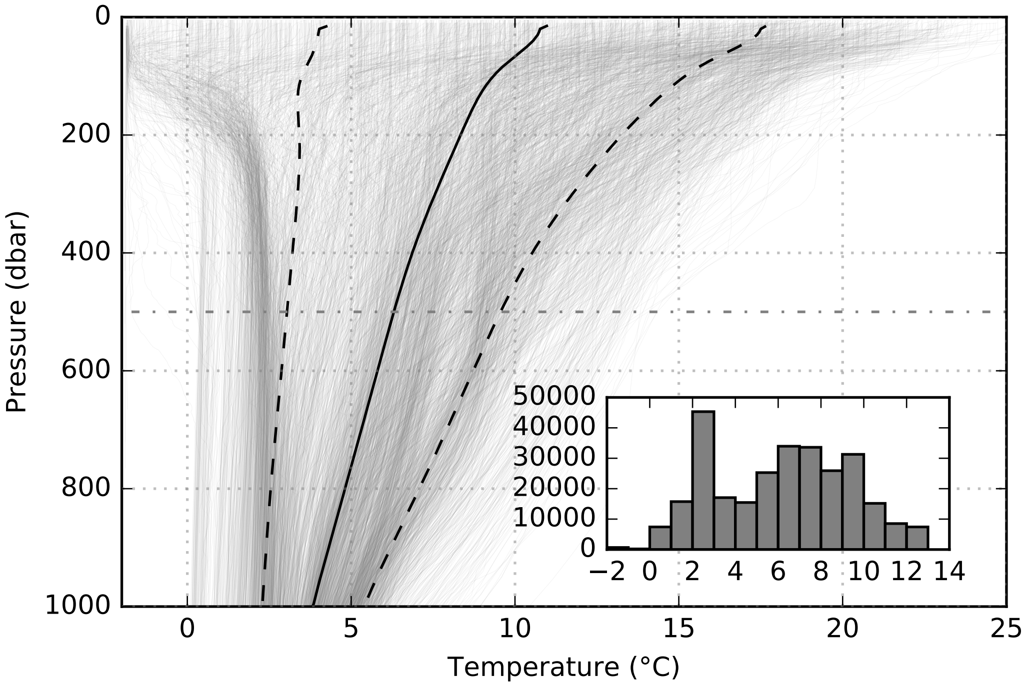

Figure 2. Plot of 10% of the Argo temperature profiles, chosen at random, in the upper 1000 dbar of the cleaned dataset, along with the mean (solid line) and the mean plus or minus one standard deviation (dashed lines) across the entire dataset. The inset figure is a histogram of temperatures at 500 dbar (marked by a dash-dot line on the main figure) with temperature on the horizontal axis and count on the vertical axis.

2.2 Gaussian mixture modeling

Gaussian mixture modeling (GMM) is a probabilistic approach for describing and classifying data. It attempts to fit (or “model" in the statistical sense) the data as a linear combination of multi-dimensional Gaussian distributions with unknown means and unknown standard deviations. Let $\mathbf{X}$ be the array of N vertical profiles, each with D pressure levels, and let $p(\mathbf{X})$ be the probability distribution function (PDF) representing the entire dataset.

GMM represents the PDF as a weighted sum of K Gaussian classes, indexed by k, i.e.:

$$p(\mathbf{X}) = \sum_{k=1}^{K} \lambda_k \mathcal{N}(\mathbf{X}; \mu_k, \Sigma_k). \tag{1}$$

Here, $\mathcal{N}(\mathbf{x}; \mu_k, \Sigma_k)$ is the multi-dimensional Gaussian PDF with a vector of means $\mu_\mathbf{k}$ and covariance matrix $\Sigma_\mathbf{k}$, i.e.:

$$\mathcal{N}(\mathbf{x}; \mu_k, \Sigma_k) = \frac{\exp\left[-\frac{1}{2}(\mathbf{x} - \mu_k)^T \Sigma_k^{-1} (\mathbf{x} - \mu_k)\right]}{\sqrt{(2\pi)^D |\Sigma_k|}}. \tag{2}$$

The probability associated with class k is $p(k) = \lambda_k$. The probability of profile $\mathbf{x}$ being in class k is $p(k|\mathbf{x}) = \lambda_k \mathcal{N}(\mathbf{x}; \mu_k, \sigma_k)/p(\mathbf{x})$, where the vector $\mathbf{x}$ is a single profile taken from the complete array $\mathbf{X}$ and $p(\mathbf{x})$ is equation (1) with a single profile $\mathbf{x}$ as the argument, i.e. a normalizing factor. Both $\mathbf{x}$ and $\mu_\mathbf{k}$ are vectors of length D.

Starting with random initial guesses for the classes, GMM proceeds by iteratively adjusting the means $\mu_\mathbf{k}$ and standard deviations $\Sigma_\mathbf{k}$ (i.e. the “parameters") of the classes in order to maximize a logarithmic measure of likelihood, i.e.:

$$\log[p(\mathbf{X})] = \sum_{i=1}^{N} \log\left[\sum_{k=1}^{K} \lambda_k \mathcal{N}(\mathbf{X}; \mu_k, \Sigma_k)\right]. \tag{3}$$

GMM uses an expectation-maximization approach, described in *Maze et al.* [2017]. This algorithm monotonically converges on a local maximum. GMM is a generalization of k-means clustering, which only attempts to minimize in-group variance by shifting the means. By contrast, GMM attempts to identify means and standard deviations, allowing for some variation about the centres of the Gaussian distributions.

In our instance of GMM, each pressure level is treated as a “dimension", and the Gaussian parameters are associated with each pressure level. However, we may not need all of these pressure levels to accurately describe the dataset, as ocean temperature changes much more rapidly in the mixed layer and thermocline than in the interior. In order to reduce the computational complexity of the problem, we transform the profile data from pressure space to an alternative space using principal component analysis (PCA). Specifically, we calculate principal components that capture a desired fraction of the vertical variability of the dataset. Each eigenvector may be thought of as a “profile type" that describes a certain amount of variance in the data with pressure (note that this is not necessarily the same thing as a “typical profile"). We calculate J principal components via the transformation:

$$\mathbf{X}(z) = \sum_{j=1}^{J} \mathbf{P}(z, j) \mathbf{Y}(j), \tag{4}$$

where z is the pressure level, J is the total number of principal components (index j), and $\mathbf{P}(z, j)$ is the transformation matrix between pressure space and principal component space. This strategy is an example of "dimensionality reduction", which is common in machine learning approaches. We find that $J = 6$ captures 99.9% of the variance in the vertical structure, which greatly reduces the number of dimensions needed to describe the Argo profile data used here, i.e. from 194 pressure levels to 6 principal components.

2.2.1 Selecting the number of classes

GMM does have one free parameter, i.e. the maximum number of classes K. In order to determine the most appropriate value for K, we applied a statistical test, namely a Bayesian Information Criterion (BIC). BIC uses an empirically formulated cost function that rewards likelihood and penalizes the number of classes K:

$$BIC(K) = -2\mathcal{L}(K) + N_f(K)\log(n), \tag{5}$$

where $\mathcal{L}$ is a measure of likelihood, n is the number of profiles used in the BIC test, and N_f is the number of independent parameters to be estimated:

$$N_f(K) = K - 1 + KD + \frac{KD(D-1)}{2}. \tag{6}$$

In this framework, the optimum value of K minimizes the BIC score. We perform a number of BIC tests, using different subsets of the data and different values of K, to estimate the distribution and variability of BIC. Using the roughly 300 km decorrelation scale of the Southern Ocean as guidance [*Ninove et al.*, 2016], we randomly select a profile from each 4° × 4° grid cell, returning 884 random profiles for each BIC test. We calculate BIC scores for each set of 884 random profiles (in principal component space) using a range of classes K from 1 to 19 (Figure 3). BIC analysis does not feature a clear minimum, but instead it suggests that the optimum value of K lies between 6 and 10.

It may seem counterintuitive that BIC does not return a single optimum value for K, but this is consistent with the nature of K as a weakly constrained free parameter that controls the level of complexity of the statistical description of the dataset. Oceanography has a rich history of expertise-driven clustering using physical and biogeochemical criteria (e.g. PV minima, oxygen minima) and the fingerprints of various processes (e.g. gyre circulation). These descriptions can be arranged into hierarchies, from coarse/simple (e.g. two-layer quasi-geostrophic models) to rich and complex (e.g. the descriptions found in *Talley* [2013]).

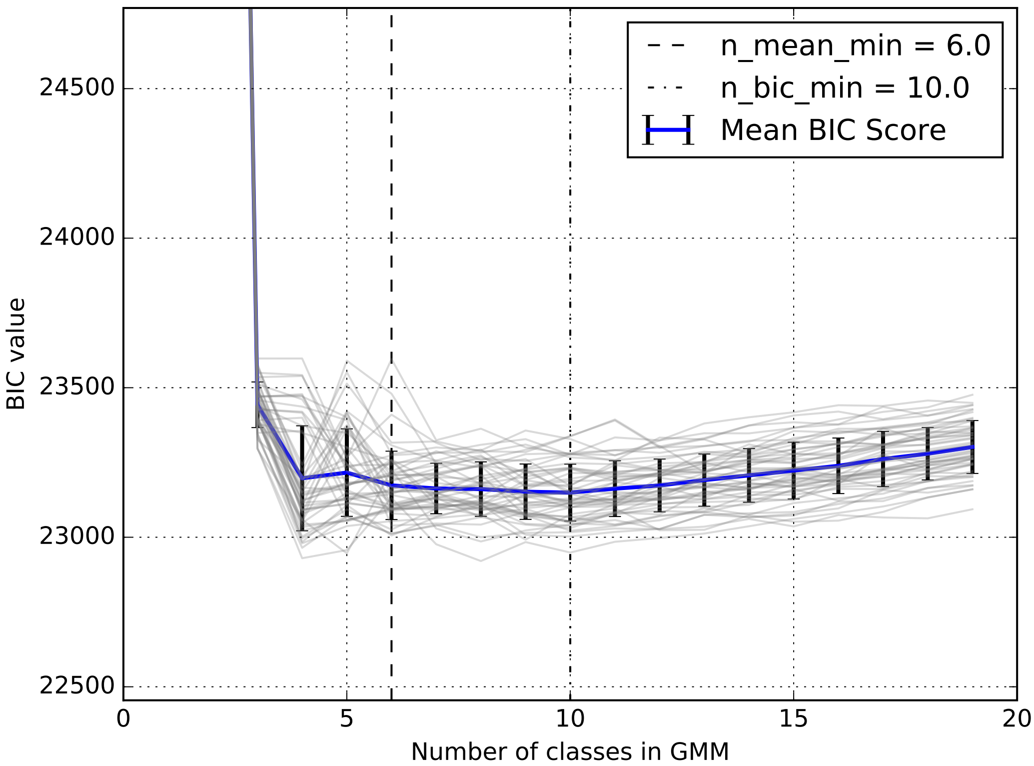

Figure 3. Bayesian Information Criteria (BIC) scores versus the specified number of classes K. Shown are the individual trials for different subsets of the temperature profile datasets (gray lines), the mean (blue line), and standard deviations computed from the profiles (error bars). The dashed vertical line represents the average of the minimums from each profile and the dash-dot vertical line represents the minimum of the average of the profiles. These two minima indicate a range of suitable values for the maximum number of classes K.

The level of detail required in the description depends on the application at hand. For example, a simple β-plane model is sufficient to explain the existence of gyres and western boundary currents; it constitutes a first-order description of gyres. Algorithmic clustering offers a robust way to traverse this hierarchy using a range of K values. Although statistical tests can be used as rough guides for choosing the number of classes, there is not necessarily a single ideal value for K. We explore the impact of K on our results in section 4.

We used a "training" dataset, a subset of the cleaned dataset, to estimate the parameters (i.e the means and standard deviations) of the GMM classes. To generate the GMM training set, we randomly selected a single profile from each $1^\circ \times 1^\circ$ bin. Each training dataset contains 12,286 profiles (roughly 4% of the cleaned dataset), distributed evenly in latitude/longitude space. We then statistically represent (i.e. 'model') the entire cleaned dataset with the fitted Gaussian model using optimized parameters. The end result is a probabilistic description of the cleaned Argo temperature profile dataset in terms of a linear combination of Gaussian distributions that vary with pressure. Each profile then has a probability distribution across the classes, and the profile is assigned to the class with the highest probability.

3 Results

In order to identify patterns in the temperature structure of the Southern Ocean, we describe the cleaned Argo temperature profile dataset as a linear combination of multi-dimensional Gaussian functions that vary with pressure, using $K = 8$ different classes. Despite the fact that GMM does not have access to the longitudes and latitudes of the profiles, it identifies spatially coherent structures, some of which are roughly demarcated by the fronts of the ACC as defined by *Kim and Orsi* [2014] (Figure 4). For ease of interpretation, we sorted the classes by mean temperature (Table 1).

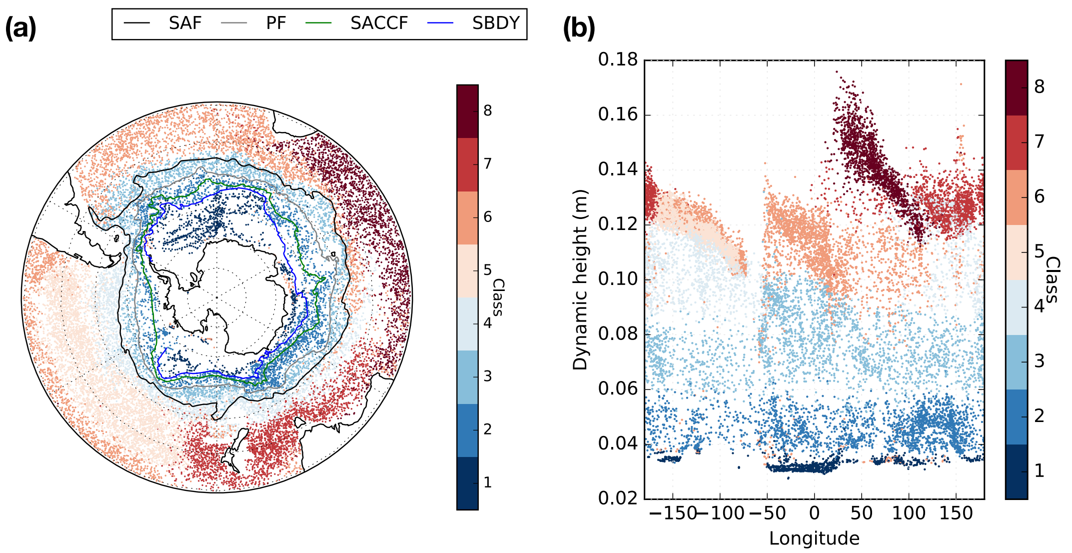

Figure 4. (a) GMM-derived class distribution for $K = 8$, shown with four fronts of the Antarctic Circumpolar Current, i.e. the Subantarctic Front (SAF), Polar Front (PF), Southern ACC Front (SACCF), and the Southern Boundary (SBDY) [*Kim and Orsi*, 2014]. (b) Class distribution shown in dynamic height space. Note that only points with posterior probability ≥ 0.9 are shown. The classes are sorted by mean temperature, from coldest ($k = 1$) to warmest ($k = 8$).

The class nearest Antarctica (class 1) extends throughout the Weddell Gyre and coastal Antarctica (Figure 4a). The mean temperature profile in this region is inverted, that is, it is colder near the surface and warmer in the interior (Figure 5). This near-Antarctic class coincides with regions of Antarctic Bottom Water (AABW) export [*Orsi et al.*, 1999], and its northern extent approximately corresponds with the classical Southern Boundary (SBDY) of the ACC [*Kim and Orsi*, 2014]. This class occupies a narrow range in dynamic height space, with a class mean and standard deviation of 3.3 ± 0.2 cm (Figure 4b); it is fairly distinct from the other classes, that is, class 1 profiles are rarely found north of the SBDY.

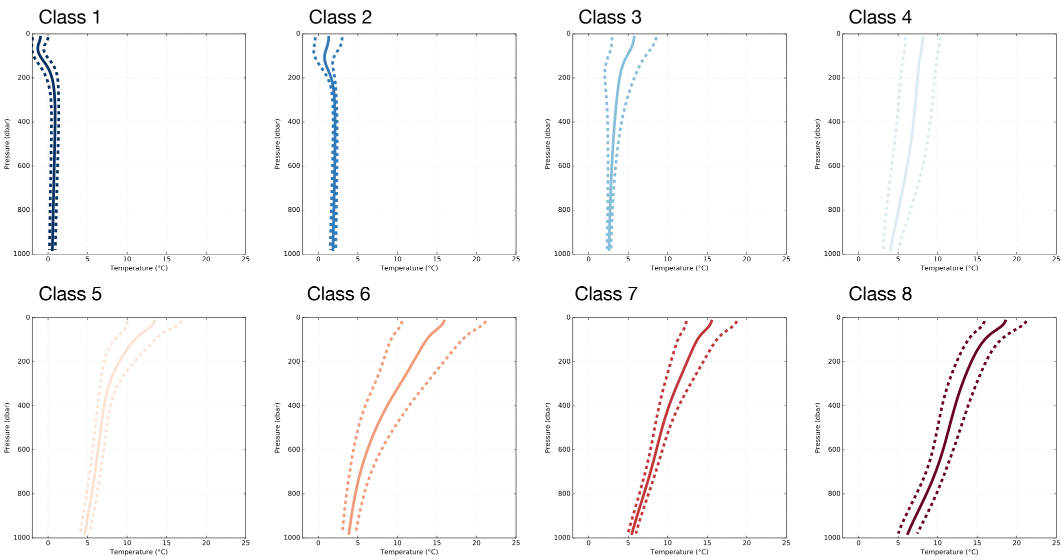

Figure 5. Temperature profile statistics, separated by class, as functions of pressure. Shown are the mean (solid lines) and the mean plus or minus one standard deviation (dashed lines) for all profiles in the indicated class.

The second coldest class (class 2) is a circumpolar class with profiles that sit north of the SBDY and south of the Polar Front (PF) across all longitudes; it is the dominant class in the dynamic height range 4-6 cm, with a class mean value of 4.8 ± 0.7 cm (Figure 4). Its mean profile is also inverted, though not as sharply as the mean profile of class 1 (Figure 5). A second circumpolar class (class 3) sits roughly north of the PF and south of the Subantarctic Front (SAF). In dynamic height space, class 3 is found between roughly 6-8 cm, except in the Atlantic sector, where it extends to roughly 10 cm. Unlike the first two classes, the mean profile of class 3 is not inverted, that is, it gets colder with pressure. The presence of these two circumpolar classes is consistent with the homogenizing influence of the ACC, which typically encourages mixing along the strong jets associated with fronts and suppresses mixing across them [*Ferrari and Nikurashin*, 2010].

The profiles assigned to class 4 are mostly located north of the SAF in the Pacific and Indian sectors, roughly coinciding with regions of Subantarctic Mode Water (SAMW) and Antarctic Intermediate Water (AAIW) formation in the Pacific Ocean and south of Australia [*Sallée et al.*, 2010]. Despite its relatively narrow range in latitude, class 4 profiles occupy a broad, distinct range in dynamic height space in the Pacific Sector, with a class mean of 11 ± 1.5 cm. The mean vertical profile associated with class 4 changes relatively gently with pressure, with no clear thermocline and a relatively large standard deviation across all pressures.

Profiles assigned to class 5 are mostly found in the Pacific Sector, in a region associated with the export of SAMW and AAIW from the surface ocean into the interior thermocline [*Iudicone et al.*, 2007; *Jones et al.*, 2016]. In contrast with class 4, class 5 occupies a relatively large range in latitude and a relatively small range in dynamic height, with a mean and standard deviation of 12 ± 0.7cm. The mean vertical profile has a clear thermocline over the upper 400 dbar of the ocean, with a standard deviation that narrows considerably with pressure.

Class 6 highlights warmer subtropical waters and is mostly found in the Atlantic and Pacific sectors; it partially extends into the Indian sector, where it sits just north of the SAF. From the surface to well into the interior, class 6 features some of the largest standard deviations of any class, suggesting that class 6 consists of a wide variety of profiles; it can potentially be split into a number of smaller classes. Classes 7 and 8 are also warmer subtropical classes, with class 7 found mostly near Australia and New Zealand and class 8 found almost exclusively in the Indian sector. The spatial extent of class 8 near South Africa suggests that the Agulhas current influences the temperature structure in that region. The mean vertical profiles of classes 7 and 8 are similar, although class 7 features higher variability near the surface and class 8 features slightly warmer surface temperatures.

As discussed in section 2, in order to make the GMM algorithm more efficient, we used PCA to reduce the number of variables required to represent the vertical structure of the temperature profiles, from over 190 pressure levels down to six principal components. Each PC is a vertical profile that can “explain", in the statistical sense of being correlated with, a fraction of the variance in temperature with pressure. Nearly 95% of the variance is explained by the first PC (i.e. PC1), and the Gaussian functions associated with PC1 are relatively distinct, capturing the broad shape of the temperature distribution (Figure 6). For higher indexed PCs, the Gaussians overlap more, but their sum still makes up a representation of the temperature distribution that is sufficiently accurate for our purposes.

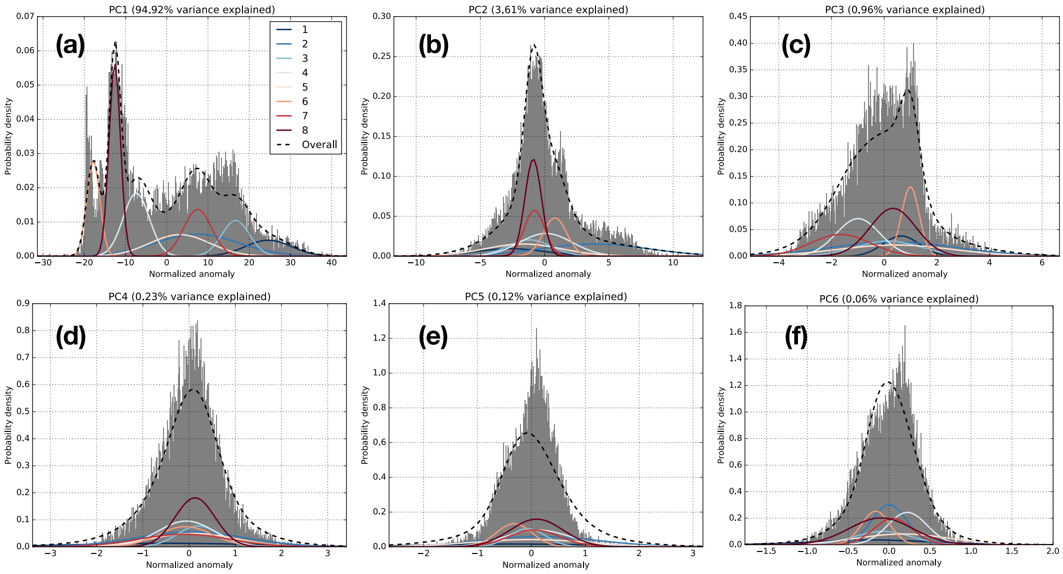

Figure 6. Probability density functions for the principal component amplitude coefficients associated with each profile, along with the Gaussian functions generated by GMM with $K = 8$ classes.

For a selected temperature profile, GMM predicts the probability distribution across all K classes. That is, it calculates the probabilities that the profile belongs to each class k. Next, the algorithm assigns the profile to the class with the highest probability. Since these probabilities are calculated with the full data set available, they are referred to as posterior probabilities. The posterior probabilities are useful in their own right, as measures of confidence in GMM's assignment of a profile to a particular class.

For our implementation of GMM on Argo temperature data, over 86% of the class assignments have posterior probabilities greater than 0.75, and over 74% of all class assignments have posterior probabilities greater than 0.9 (Table 2). Class 1 features an especially high percentage of very high posterior probabilities; over 90% of assignments into class 1 have posterior probabilities greater than or equal to 0.9. Outside of the Weddell Gyre, we find the lowest posterior values in the Ross Sea and a few near-coastal areas (Figure 7). Classes 2 and 3 also feature high posterior probabilities, for which over 70% of assignments have values greater than or equal to 0.9. For both of these classes, we find relatively low posterior probabilities upstream of Kerguelen Island (KI), clustered around the PF.

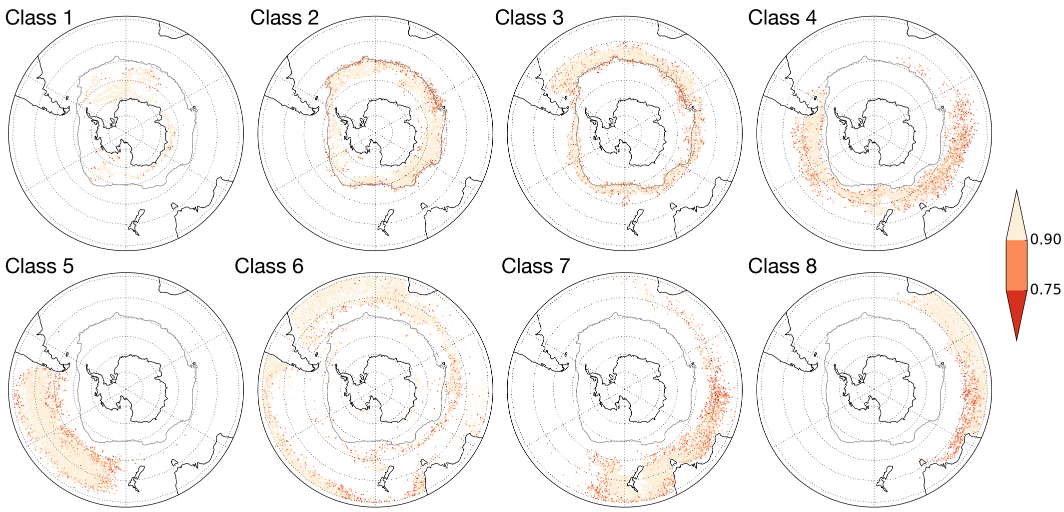

Figure 7. Posterior probabilities for each class assignment, given the full cleaned dataset, shown together with the PF for reference [*Kim and Orsi*, 2014].

Although over 60% class 4 profiles have posterior values greater than or equal to 0.9, class 4 features some relatively low posterior values compared with the other classes, especially in the Indian sector north of the SAF. In the Pacific sector, we find relatively low posteriors along the boundary between classes 4 and 5. Class 5 has a core of profiles with posterior values greater than or equal to 0.9, with relatively lower values all along its boundary. We find similar patterns for classes 6-8, except in the Indian sector between 60-120$^\circ E$, north of the SAF. This region, which is downstream of Kerguelen Plateau, is characterized by relatively low posterior values for classes 4, 7, and 8. The area around KI is affected by upwelling, mixing, and the confluence of the Agulhas Retroflection and the ACC [*Sallée et al.*, 2010], and it also features relatively high eddy diffusivities [*Klocker and Abernathey*, 2014]. The profiles in that area are influenced by a number of competing processes and may be difficult to unambiguously separate into clear groups when using a value of K appropriate for the entire Southern Ocean. In general, although GMM performs well in all ocean basins, in terms of clear class separation with high posterior probabilities, its performance is somewhat weaker in the Indian sector.

4 Discussion

4.1 Sensitivity to number of classes K

In section 2, we estimated that the optimum number of classes K lies between 6 and 10. The weak constraint suggested by BIC allows for some tuning depending on the desired level of complexity in the description of the dataset. Using $K = 6$ classes is sufficient to capture most of the large-scale structures identified in the $K = 8$ case, but there are some significant differences (Figure 8). Specifically, there is one fewer circumpolar class, as classes 1-3 are reduced to classes 1-2 that sit roughly on either side of the PF. In the Pacific sector, classes 4 and 5 merge into the new class 4. In the Indian sector, classes 7-8 merge into the new class 6 that sits north of the SAF and south of Australia. We see that the overall description of ocean structure is simpler with $K = 6$; it is still a physically reasonable description of ocean temperature structure, with circumpolar classes and clusters that span the major basins, but it lacks some of the subtleties found in the $K = 8$ map.

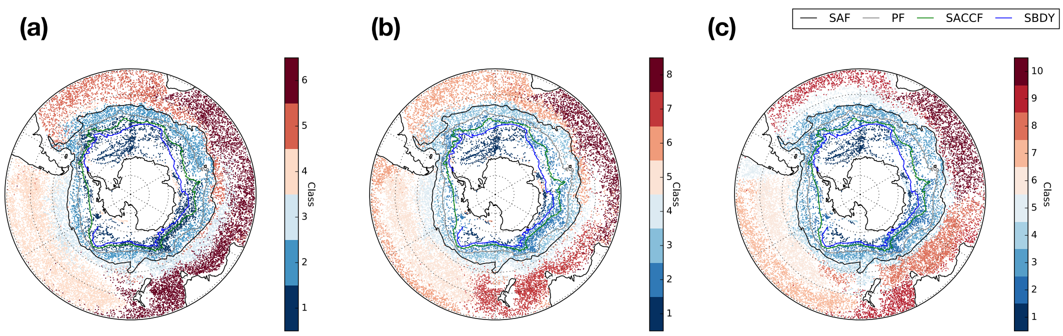

Figure 8. Comparison of GMM-derived classes, shown for (a) 6 classes, (b) 8 classes, and (c) 10 classes, along with fronts of the ACC [*Kim and Orsi*, 2014].

As expected, the $K = 10$ case features more structure than the $K = 8$ case, and it is still a physically reasonable distribution. Classes 1-3 are still near-Antarctic or circumpolar classes; the additional structure all appears north of the SAF. In the Pacific basin, the boundary between the $K = 8$ classes 5 and 6 and the $K = 10$ classes 6 and 7 is shifted polewards, and a new class 5 is found along the Eastern Pacific, along the South American coast. The $K = 10$ class 8 is found south of Australia, which in the $K = 8$ class is not a distinct class. Interestingly, in the $K = 10$ case we find more profiles above 0.9 posterior probability in the Indian sector, specifically in the region north of the SAF and between the longitudes of 60-120°E. Increasing K allowed for a more likely set of class assignments in this previously troublesome region. So, regions of low posterior probabilities may suggest a need for a higher value of K.

4.2 Functional PCA

In this work, we used PCA to reduce the dimensionality of our Argo temperature profile dataset. An alternative approach is to use functional principal component analysis (fPCA), in which PCA is performed on functions instead of the original data. In *Pauthenet et al.* [2017], the authors represent vertical temperature and salinity profiles from the Southern Ocean State Estimate [*Mazloff et al.*, 2010] as linear combinations of B-spline basis functions and apply fPCA to the resulting spline functions. They use the principal components to examine large-scale structures such as fronts in the Southern Ocean. Their approach offers another objective way to define water mass boundaries and could be used in concert with the GMM approach outlined in this work. This could offer a useful way to introduce salinity into the GMM analysis, which is especially relevant for stratification south of the PF [*Pollard et al.*, 2002].

5 Conclusions

We applied Gaussian mixture modeling (GMM), an unsupervised classification scheme, to Southern Ocean Argo temperature data above 1000 dbar. Without using longitude or latitude information, GMM identified spatially coherent patterns in the vertical temperature structure. The GMM-derived classes broadly coincide with large-scale circulation and stratification features, including regions of AABW formation and upwelling (i.e. adjacent to Antarctica), the ACC, formation and export pathways of SAMW and AAIW, subtropical gyre circulation, and the Agulhas Current and associated retroflection. The class boundaries broadly coincide with several classically-defined fronts of the ACC, and the circumpolar classes mostly occupy distinct regions in dynamic height space, indicating that GMM has identified physically distinct profile types using only vertical temperature data. Posterior probability distributions indicate regions where the classes are distinct and statistically separate, whereas regions with low posterior probability indicate boundaries between classes and/or regions of mixing influenced by a number of different temperature structures. GMM may offer an alternative, complementary method for classification of Southern Ocean density structures, and it is potentially useful for objectively and automatically comparing structures across different observational and modeling datasets.

Class	Number of profiles	Mean	Std. dev.	Min.	Max.
1	10680	0.48	0.81	-2.11	2.52
2	33031	1.83	0.72	-1.87	8.89
3	40268	3.38	1.50	-1.82	19.70
4	39619	6.36	2.24	-1.85	17.17
5	48252	7.32	2.56	2.76	25.37
6	48770	8.22	4.49	-1.88	27.56
7	38682	9.70	3.07	3.25	27.11
8	25130	11.57	3.43	3.56	28.08

Table 1. Temperature statistics for each class, using values from every pressure level. All temperature statistics are shown in °C. The classes have been sorted by mean temperature, calculated using values from all pressure levels.

Class	[0.0, 0.50)	[0.50, 0.75)	[0.75, 0.9)	[0.9, 1.0]
1	<1	4	4	91
2	<1	11	11	77
3	<1	14	16	70
4	1	18	20	61
5	<1	7	8	84
6	<1	9	8	82
7	<1	19	17	64
8	<1	13	12	75

Table 2. Posterior probabilities for each class, divided into four unequal intervals. Each row shows the percentage of profiles assigned to that class with posterior probabilities in the indicated range.

Acronyms

AABW Antarctic Bottom Water

AAIW Antarctic Intermediate Water

ACC Antarctic Circumpolar Current

ARGO Array for Real-time Geostrophic Oceanography

BIC Bayesian Information Criterion

fPCA Functional principal component analysis

GDAC Global Data Assembly Center

GMM Gaussian mixture modeling

PC Principal component

PCA Principal component analysis

PDF Probability distribution function

SAMW Subantarctic Mode Water

Acknowledgments

This study is supported by grants from the Natural Environment Research Council (NERC), including [1] The North Atlantic Climate System Integrated Study (ACSIS) [grant NE/N018028/1 (authors DJ, ES)] and [3] Ocean Regulation of Climate by Heat and Carbon Sequestration and Transports (ORCHESTRA) [grant NE/N018095/1 (authors ES, AM)]. HH was funded by a NERC DTP Research Experience Placement over the summer of 2017 [grant NE/L002434/1]. Argo floats data and metadata from the Global Data Assembly Centre (Argo GDAC), `http://doi.org/10.17882/42182`. The analysis software used in this manuscript was written using Python and the *scikit-learn* machine learning library (`http://scikit-learn.org/stable/`). The scripts we used are available via github (`https://github.com/DanJonesOcean/OceanClustering`). DJ thanks Chris Lowder for python support. We are grateful to YS Kim for providing us with Southern Ocean front position data. Finally, we thank two anonymous reviewers, whose feedback greatly improved the quality of our work.

References

Ferrari, R., and M. Nikurashin (2010), Suppression of eddy diffusivity across jets in the Southern Ocean, *Journal of Physical Oceanography*, *40*, 1501–1519, doi:10.1175/2010JPO4278.1.

Fletcher, S. M., N. Gruber, A. R. Jacobson, S. C. Doney, S. Dutkiewicz, M. Gerber, M. Follows, F. Joos, K. Lindsay, D. Menemenlis, A. Mouchet, S. A. Müller, and J. L. Sarmiento (), Inverse estimates of anthropogenic CO2 uptake, transport, and storage by the ocean, *Global Biogeochemical Cycles*, *20*, doi:10.1029/2005gb002530.

Frölicher, T. L., J. L. Sarmiento, D. J. Paynter, J. P. Dunne, J. P. Krasting, and M. Winton (2015), Dominance of the Southern Ocean in Anthropogenic Carbon and Heat Uptake in

CMIP5 Models, *Journal of Climate*, *28*(2), 862–886, doi:10.1175/jcli-d-14-00117.1.

Iudicone, D., K. Rodgers, R. Schopp, and G. Madec (2007), An exchange window for the injection of Antarctic Intermediate Water into the South Pacific, *Journal of Physical Oceanography*, *37*, 31–49, doi:http://dx.doi.org/10.1175/JPO2985.1.

Jones, D. C., A. J. S. Meijers, E. Shuckburgh, J.-B. Sallée, P. Haynes, E. K. McAufield, and M. R. Mazloff (2016), How does Subantarctic Mode Water ventilate the Southern Hemisphere subtropics?, *Journal of Geophysical Research - Oceans*, *121*(9), 6558–6582, doi:10.1002/2016jc011680.

Kim, Y. S., and A. H. Orsi (2014), On the Variability of Antarctic Circumpolar Current Fronts Inferred from 1992–2011 Altimetry*, *Journal of Physical Oceanography*, *44*(12), 3054–3071, doi:10.1175/JPO-D-13-0217.1.

Klocker, A., and R. Abernathey (2014), Global Patterns of Mesoscale Eddy Properties and Diffusivities, *Journal of Physical Oceanography*, *44*(3), 1030–1046, doi:10.1175/jpo-d-13-0159.1.

Lumpkin, R., and K. Speer (2007), Global ocean meridional overturning, *Journal of Physical Oceanography*, *37*, 2550–2562, doi:10.1175/JPO3130.1.

Maze, G., H. Mercier, R. Fablet, P. Tandeo, M. L. Radcenco, P. Lenca, C. Feucher, and C. Le Goff (2017), Coherent heat patterns revealed by unsupervised classification of Argo temperature profiles in the North Atlantic Ocean, *Progress in Oceanography*, *151*, 275–292, doi:10.1016/j.pocean.2016.12.008.

Mazloff, M. R., P. Heimbach, and C. Wunsch (2010), An Eddy-Permitting Southern Ocean State Estimate, *Journal of Physical Oceanography*, *40*(5), 880–899, doi:10.1175/2009jpo4236.1.

Ninove, F., P. Y. Le Traon, E. Remy, and S. Guinehut (2016), Spatial scales of temperature and salinity variability estimated from Argo observations, *Ocean Science*, *12*(1), 1–7, doi:10.5194/os-12-1-2016.

Orsi, A. H., G. C. Johnson, and J. L. Bullister (1999), Circulation, mixing, and production of Antarctic Bottom Water, *Progress in Oceanography*, *43*(1), 55–109, doi:10.1016/s0079-6611(99)00004-x.

Pauthenet, É., F. Roquet, G. Madec, and D. Nerini (2017), A linear decomposition of the Southern Ocean thermohaline structure, *Journal of Physical Oceanography*, *47*, 29–47, doi:10.1175/JPO-D-16-0083.s1.

Pollard, R., M. Lucas, and J. Read (2002), Physical controls on biogeochemical zonation in the Southern Ocean, *Deep Sea Research Part II*, *49*(16), 3289–3305, doi:10.1016/S0967-0645(02)00084-X.

Sallée, J., E. Shuckburgh, N. Bruneau, A. Meijers, T. Bracegirdle, Z. Wang, and T. Roy (2013), Assessment of Southern Ocean water mass circulation and characteristics in CMIP5 models: historical bias and forcing response, *Journal of Research: Oceans*, *118*, 1830–1844, doi:10.1002/jgrc.20135.

Sallée, J.-B., K. Speer, S. Rintoul, and S. Wijffels (2010), Southern Ocean Thermocline Ventilation, *Journal of Physical Oceanography*, *40*(3), 509–529, doi:10.1175/2009jpo4291.1.

Talley, L. (2013), Closure of the Global Overturning Circulation Through the Indian, Pacific, and Southern Oceans: Schematics and Transports, *Oceanography*, *26*(1), 80–97, doi:10.5670/oceanog.2013.07.